

Gas-phase microactuation using kinetically controlled surface states of ultrathin catalytic sheets

Nanqi Bao^{a,1}, Qingkun Liu^{b,1,2}, Michael F. Reynolds^b, Marc Figueras^c, Evangelos Smith^c, Wei Wang^{b,d}, Michael C. Cao^e, David A. Muller^{e,f}, Manos Mavrikakis^c, Itai Cohen^{b,f}, Paul L. McEuen^{b,f}, and Nicholas L. Abbott^{a,3}

Edited by Alexis Bell, University of California, Berkeley, CA; received December 23, 2022; accepted March 14, 2023

Biological systems convert chemical energy into mechanical work by using protein catalysts that assume kinetically controlled conformational states. Synthetic chemomechanical systems using chemical catalysis have been reported, but they are slow, require high temperatures to operate, or indirectly perform work by harnessing reaction products in liquids (e.g., heat or protons). Here, we introduce a bioinspired chemical strategy for gas-phase chemomechanical transduction that sequences the elementary steps of catalytic reactions on ultrathin (<10 nm) platinum sheets to generate surface stresses that directly drive microactuation (bending radii of 700 nm) at ambient conditions (T = 20 °C; Ptotal = 1 atm). When fueled by hydrogen gas and either oxygen or ozone gas, we show how kinetically controlled surface states of the catalyst can be exploited to achieve fast actuation (600 ms/cycle) at 20 °C. We also show that the approach can integrate photochemically controlled reactions and can be used to drive the reconfiguration of microhinges and complex origami- and kirigami-based microstructures.

chemomechanical | catalysis | kinetic surface states | microactuator

Electrochemical systems permit direct and efficient conversion of chemical energy to electrical energy [e.g., fuel cells (1)]. In contrast, harnessing the chemical potential energy of fuels to perform mechanical work in engineered devices typically involves indirect transduction pathways in liquids [e.g., using localized effects of heat (2, 3) or chemical products (4) to drive phase transitions or generate osmotic pressure differences]. Because heat and chemical concentration gradients dissipate quickly (<1 s) on the micrometer scale, such approaches do not scale well to the actuation of microdevices. Nature overcomes this limitation by performing direct chemical-to-mechanical transduction with catalytic motor proteins: The conformational states of the proteins change during kinetically controlled catalytic cycles to perform work (5). Attempts to recapitulate these principles through adsorbate-induced surface stresses on metallic surfaces have been reported (Fig. 1A), but the actuator responses are slow (>10 mins) (6), are small in magnitude (curvatures of $<10^{-4} \, \mu m^{-1}$) (7–10), or require operation at high temperatures (250 °C) (11) (SI Appendix, Text and Table S1). To overcome these limitations, herein, we show how materials engineered on the micro- and nano-scale enable designs of micromachines for energy transduction in a limit where actuator bending energies are comparable to the free energies of surface reactions. The approach is also applicable to gas-phase (dry) microactuation.

Results

Our surface-catalyzed chemical actuators (SCAs) were designed to harness the free energy of catalytic reactions between H_2 and either O_2 or O_3 on Pt (12–15 and *SI Appendix*). Initially, as shown in Fig. 1B, we cycled the Pt surfaces of our SCAs between H_2 and $O_2/$ O₃ to generate surface states and curvatures of the actuator that are characterized by adsorbed hydrogen (H*) or adsorbed oxygen (O*)/platinum oxide (PtO_x), respectively (state 1 and state 2). Importantly, however, we found that kinetically controlled states of the actuator (transient state in Fig. 1B), which are set by the relative rates of elementary surface reactions on the Pt surface, can be used to achieve actuator responses that are faster and larger in magnitude than those achieved using the equilibrated end states (i.e., H* and O^*/PtO_x ; states 1 and 2 in Fig. 1*B*).

The SCAs were fabricated from 7.5 nm-thick films of Pt [dominated by (111) facets covered with 0.25 monolayer (ML) of O* in air; SI Appendix, Fig. S2] that were capped on one side by 2 nm-thick passivating layers of TiO₂ (Fig. 1C) (16, 17). The SCAs were fabricated as hinges between fixed SiO₂ panels and rotating SiO₂ panels (20 μm length × $30 \ \mu m$ width \times 500 nm thickness) to enable measurement of bending of the SCAs

Significance

Chemomechanical transduction in engineered devices typically involves indirect transduction pathways, using localized physical effects of reaction products to perform work in liquids (e.g., thermal or chemical products to drive phase transitions or generate osmotic pressure differences, respectively). Those approaches do not work in dry environments, and they are challenging to scale to microdevices due to rapid dissipation of heat or chemical gradients on the micrometer scale. Inspired by nature's use of catalytic motor proteins to perform direct chemomechanical transduction during kinetically controlled conformations, here, we describe how surface states, accessed by controlling the kinetics of surface reactions using an ultrathin (<10 nm) synthetic catalyst sheet, can be used to achieve direct, fast, and microscale chemomechanical transduction using hydrogen gas at room temperature.

The authors declare no competing interest.

This article is a PNAS Direct Submission.

Copyright © 2023 the Author(s). Published by PNAS. This article is distributed under Creative Commons Attribution-NonCommercial-NoDerivatives License 4.0 (CC BY-NC-ND).

¹N.B. and Q.L. contributed equally to this work.

²Present address: National Key Lab of MicroNano fabrication Technology, Shanghai Jiao Tong University, Shanghai 200240,

³To whom correspondence may be addressed. Email:

This article contains supporting information online at https://www.pnas.org/lookup/suppl/doi:10.1073/pnas.2221740120/-/DCSupplemental.

Published May 1, 2023.

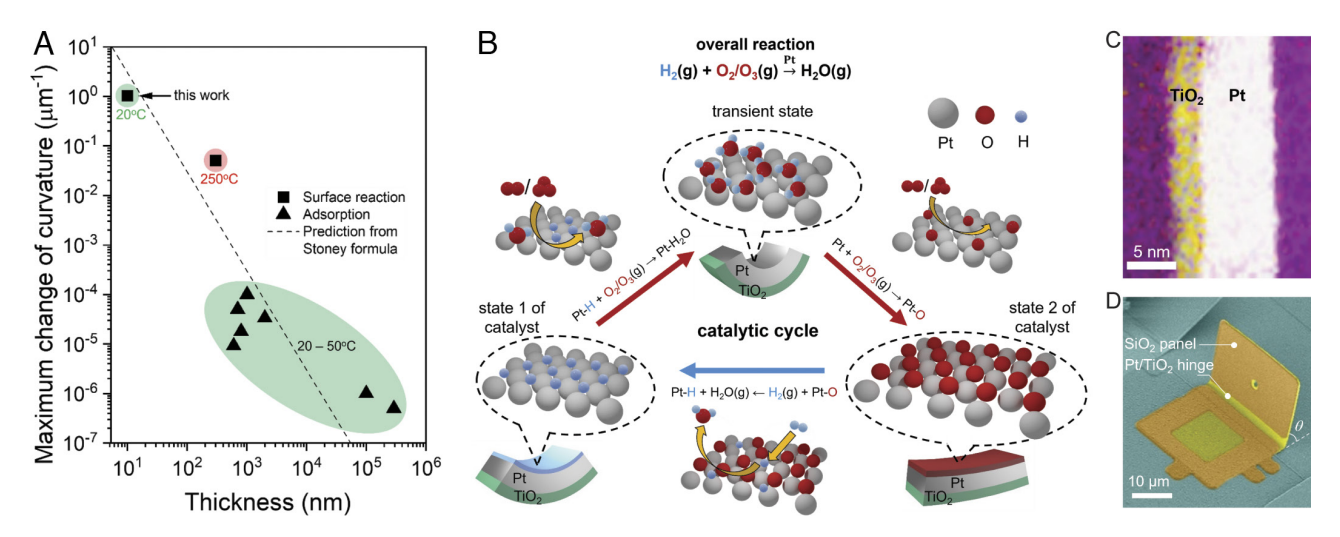


Fig. 1. Mechanism, composition, and structure of surface-catalyzed chemical actuators (SCAs). (A) Performance of chemomechanical systems based on metal surfaces that operate in gas environments plotted as a function of thickness and maximum change in the curvature of the actuated surfaces. The past studies indicated on the plot are detailed in SI Appendix, Text and Table S1. The dashed line is a prediction of the Stoney formula (see main text). (B) Schematic illustration of the cycling of the catalytic surface of the SCA used in our study. States 1 and 2 of the Pt(111) surface are accessed by equilibration against H₂ (state 1) and either O_2 or O_3 (state 2). In contrast, the transient state of the Pt(111) surface shown in B is a kinetic surface state of the actuator. The transient state is observed when going from state 1 to state 2 but not state 2 to state 1 because different chemical species are present on the SCA surface during the forward and reverse transformations (SI Appendix, Text). (C) A false-color transmission electron micrograph (TEM) of the cross-section of a SCA: 7.5 nm of platinum (white) capped on one side by 2 nm TiO₂ film (yellow) grown on the silicon wafer (magenta, *Left*). (D) A false-color scanning electron micrograph (SEM) of a SCA exposed to ambient air following fabrication.

(Fig. 1D). Initially, the SCAs were curved toward the Pt surface due to stresses introduced during fabrication. During chemical actuation, we quantified changes in bending curvature of each SCA hinge by measuring changes in the projected length of the SiO_2 panels (viewed from above; Fig. 2 A and B).

Initial experiments were performed to determine the magnitude of actuation of the SCAs following sequential exposure to H₂ and then O_2 (T = 20 °C; P_{total} = 1 atm). Inspection of Fig. 2 A and B reveals that exposure of SCAs to 2 v% H_2 and then 50 v% O_2 led to the sequential closing and opening of the hinge. We quantified the overall change in curvature of the hinge to be 0.2 μm⁻¹ (from t = 0 s to t = 20 s in Fig. 2*C*). This is four orders of magnitude larger than that reported previously for chemomechanical devices that operate at ambient temperature (Fig. 1A) and is the first key result of this study. In addition, when examining the dynamics of the response to O_2 (t = 20 s and t = 160 s in Fig. 2C), we found the SCAs to exhibit a greatly accelerated actuation (<1 s) to a transient curvature of 0.35 µm⁻¹ (*Inset* in Fig. 2C), a value that lies outside the two end-state curvatures achieved upon equilibration of the SCAs against H₂ or O₂.

To understand the dynamic response of the SCAs to O_2 , we used density functional theory (DFT)-based calculations to compute the potential energy diagrams for the reaction of O₂ with 1 ML H* on Pt(111) [the predicted saturation coverage of H* induced by exposure to H₂(g) under our experimental conditions (SI Appendix, Fig. S5)]. We found that the pathway with the lowest activation energy barrier (E_b) starts with H*-assisted O₂ dissociation (18) and ends with formation of H₂O* (via surface intermediates OOH*, HOOH*, and OH*; Fig. 2E black line). Because the highest E_b in the pathway (0.37 eV for decomposition of HOOH*) is smaller than the desorption energy (E_{des}) of H_2O^* (0.47 eV in Fig. 2E), these calculations predict that the Pt surface will assume a transient state that is characterized by adsorbed H₂O* but minimal coverage of H* and O* (a schematic illustration is shown in Fig. 1B; direct dissociation of O₂ is slow, as shown below). Because our calculations also indicate that H₂O* does not strain the Pt(111) surface as much as O* and H*

(chemisorbed O* or H* bind to surface Pt atoms and cause an increase in the Pt-Pt distance; SI Appendix, Fig. S5), we interpret the high transient SCA curvature observed in our experiments following exposure to O_2 (at t = 24 s in the *Inset* in Fig. 2C) to be a kinetically controlled state of the SCA dominated by adsorbed H₂O* (Fig. 2D). This conclusion is supported by control experiments revealing that H₂O has no measurable influence on actuation (SI Appendix, Fig. S6). The gradual decrease in curvature that follows the transient SCA state arises from a slow accumulation of O* on the Pt surface via direct dissociation of O_2 [E_b = 0.47 eV in *SI Appendix*, Fig. S5; saturation coverage of 0.25 ML of O* at 300 K (19)], as supported by X-ray photoelectron spectroscopy (XPS) measurements (O1s signal; SI Appendix, Fig. S7A). We note here that our analysis does not include the effects of surface defects (20) or strain (21) on reaction kinetics and thermodynamics, which may also influence SCA dynamics.

Next, to understand the monotonic dynamic response of the SCA to H₂ (Fig. 2C; blue), we calculated potential energy diagrams for H₂ dissociation on the 0.25 ML O*-covered Pt(111) surface. Although H₂ dissociation on Pt atoms directly interacting with O* (labeled with red stars in Fig. 2F) involves a significant activation energy barrier ($E_b = 0.46$ to 0.58 eV; *SI Appendix*, Fig. S5*D*), we calculated that Pt atoms not directly interacting with O* (labeled with black stars in Fig. 2F) dissociate H₂ without a barrier (Fig. 2F). This leads us to predict accumulation of H* on the SCA surface prior to removal of all O* (22), a prediction that is consistent with our observation of a monotonic change in SCA curvature following exposure to H₂ (Fig. 2C). Overall, the results above reveal that the kinetics of elementary surface reactions can dictate the surface states of SCAs, allowing the actuator to rapidly access curvatures that lie outside those measured at equilibrated coverages of adsorbates.

Armed with this understanding, we demonstrated that the above-described kinetically controlled surface states of the SCA can also be accessed at steady state by cofeeding mixtures of gaseous \boldsymbol{H}_2 and O_2 (Fig. 3A). In particular, when C_{O_2}/C_{H_2} = 10 to 15, the SCA exhibited curvatures comparable to the transient state at t = 24 s in

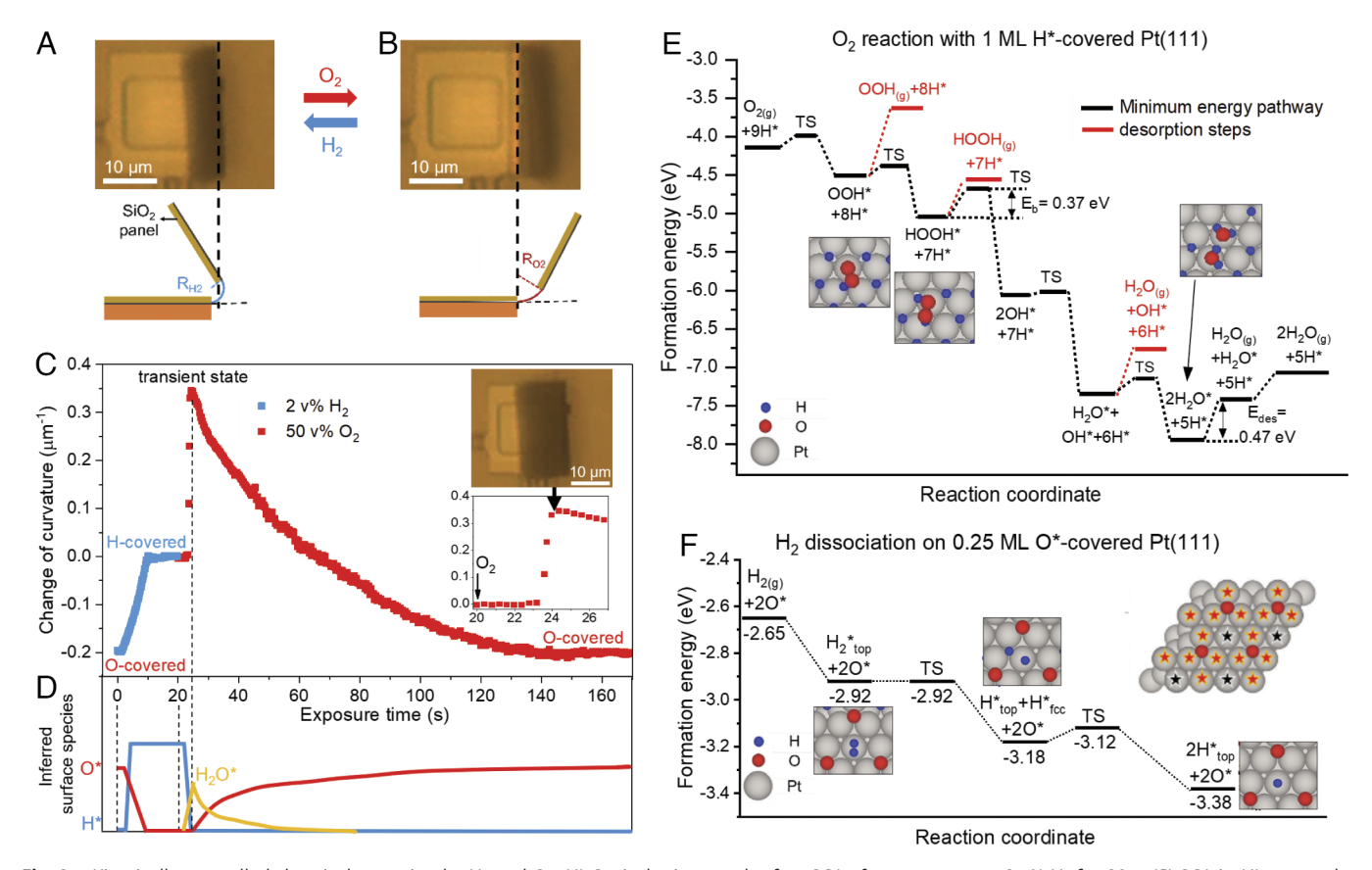


Fig. 2. Kinetically controlled chemical actuation by H_2 and O_2 . (*A*) Optical micrograph of an SCA after exposure to 2 v% H_2 for 20 s. (*B*) SCA in (*A*) exposed to 50 v% O_2 for 150 s. Schematic illustrations of the SCA (side view) are shown below the images. (*C*) Change of curvature of an SCA (pretreated with 50 v% O_2 for 150 s) when exposed to 2 v% H_2 (starting at t = 0 s; blue squares) and then 50 v% O_2 (red squares). The *Insets* show the actuation between t = 20 s and t = 27 s and a micrograph of the SCA at t = 24 s. All measurements were performed at room temperature. (*D*) Schematic illustration of the inferred qualitative trend in O_2 , H_2 , and H_2 0° coverage based on experimental observations. (*E*) and (*F*) reaction steps and their energetics calculated with DFT for the reaction of: O_2 with the 1 ML H*-covered Pt(111) (reference state is $O_{2(g)} + 4.5 H_{2(g)}$) and H_2 dissociation on the 0.25 ML O*-covered Pt(111) (reference state is $O_{2(g)} + H_{2(g)}$), respectively. Transition states are labeled with "TS."

Fig. 2C, consistent with a state of Pt surface of the SCA that is dominated by H_2O^* . Guided by this finding, and our observations that the kinetics of removal of H^* by O_2 (Fig. 2C) and H_2 dissociation are both rapid on the SCAs, we predicted that rapid actuation of SCAs should be possible by cycling between H_2 and $10:1~O_2-H_2$ mixtures. Our experiments confirmed this prediction, revealing that the SCA can be driven through a full cycle of actuation within 600 ms (limited by mass transport) at an average rate of actuation of $0.8~\mu m^{-1}/s$ (Fig. 3 B and C and Movie S1). This is the second key result of our study: The kinetics of select elementary reactions occurring on the surfaces of ultrathin catalyst sheets can be exploited to design fast, reversible chemical actuators even if the overall reaction is slow to reach equilibrium.

We also explored the use of other chemical species to actuate SCAs. Because $\rm O_3$ rapidly generates $\rm O^*$ on $\rm Pt(111)$ which then forms $\rm PtO_x$ at room temperature [equivalent to 2.4 ML of $\rm O^*$ (15)], we exposed SCAs pretreated with 2 v% $\rm H_2$ to 1,290 \pm 40 ppm $\rm O_3$. We observed the SCA to exhibit a fast response consistent with a kinetically controlled surface state that relaxed to yield an overall change in curvature of 0.7 μm^{-1} (SI Appendix, Text and Fig. S8 and Movie S2). We measured no loss of actuation of SCAs over 20 cycles of sequential exposure to $\rm O_3$ and $\rm H_2$ (SI Appendix, Fig. S8), which we showed using XPS to coincide with the formation and removal of $\rm PtO_x$ (SI Appendix, Fig. S7B). Fig. 4A reveals that the SCA curvature changes linearly with the $\rm PtO_x$ thickness (measured using electrical conductivity), in agreement with the Stoney formula:

$$\Delta \kappa = \frac{-6\left(1 - v_s\right) E_{ox} \varepsilon_{ox}}{E_s} \frac{h_{ox}}{h_s^2},$$

where $\Delta \kappa$ is the change of curvature resulting from exposure to H_2 or O_3 , and h_{ox} , v_s , E_s , h_s , E_{ox} , and ε_{ox} are the PtO_x thickness, overall Poisson's ratio, overall Young's modulus, thickness of the Pt/TiO₂ bilayer, and Young's modulus and strain in the Pt oxide layer, respectively (SI Appendix, Text). The measured SCA curvature matches the Stoney formula with a best-fit value of strain of PtO_x of 1.2% and an SCA efficiency of 0.6% (SI Appendix, Text). After exposure to O₃ and transfer to He, we found that the SCAs exhibited constant curvature for over 13 h (SI Appendix, Fig. S9), consistent with prior studies demonstrating that thermal decomposition of PtO_x on Pt(111) does not occur at significant rates below 680 K (23). This is our third key result: SCAs can function as shape-memory microactuators (17) using chemical fuels such as O₃ that generate surface states (e.g., PtO_y) that are long lived at ambient temperatures. We comment here that our observation of shape-memory behavior in the absence of an ongoing reaction indicates that the heat of reaction is not responsible for the response of the SCAs. Additionally, temperature changes of thousands of K would be needed to achieve a strain of 1.2% if the actuation was driven by the heat of reaction (SI Appendix, Text). We also found SCA actuation to be exquisitely sensitive to O₃ concentration, with parts-per-billion concentrations driving actuation (SI Appendix, Text and Fig. S10). This result hints at the

0.00

0

100

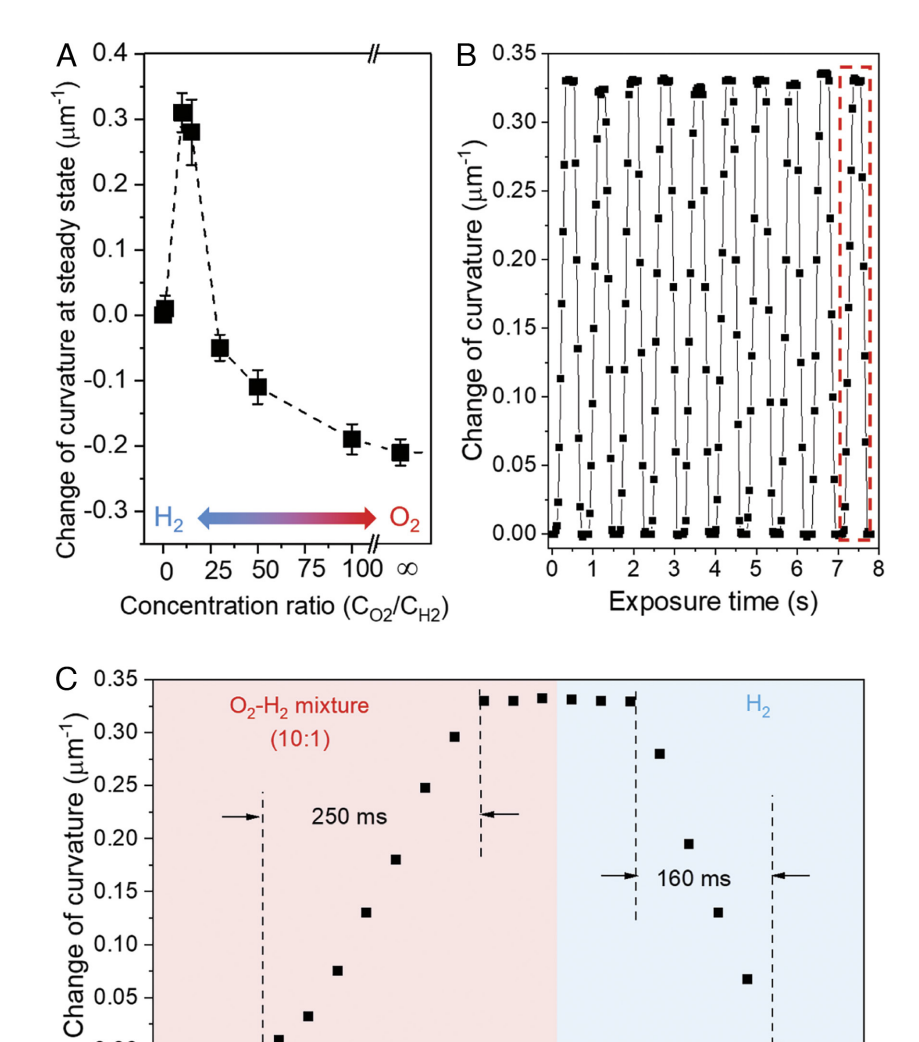


Fig. 3. Rapid actuation by O_2 – H_2 mixtures. (*A*) Steady-state curvature of an SCA exposed to the indicated gaseous mixtures of H_2 and O_2 for 5 min. The concentration of H_2 in the mixture was 1 v%, except for the 100:1 mixture which contained 0.5 v% H_2 . (*B*) Reversible actuation of an SCA driven by cycles of exposure to a gaseous 10:1 O_2 – H_2 mixture and then H_2 . (*C*) Dynamic response of the SCA in the cycle highlighted by the red dashed rectangle in (*B*). All measurements were performed at room temperature.

potential utility of SCAs to scavenge useful work from anthropogenic sources of O_3 [e.g., photochemical smog (0.1 to 0.5 ppm) (24) or fumigants (10 ppm) (25)].

300

200

400

Exposure time (ms)

500

600

Our SCAs are fabricated using standard semiconductor processes, which enables their scalable integration into microdevices with complex structures containing multiple SCAs (Fig. 4 B–D). Kirigami-based rotation microstages were fabricated using the design shown in Fig. 4B and transferred to air prior to actuation. Valley folds fabricated with Pt/TiO2 active hinges (green shaded regions in Fig. 4B) were actuated by exposure to 2 v% H₂, resulting in a translational stroke of 10 µm to 20 µm perpendicular to the substrate and a clockwise rotation of $\pi/4$ rad (Fig. 4 C and D and Movie S3). Chemical actuation was used to fold flat surfaces into programmed shapes (Fig. 4 E-G). The *Insets* in Fig. 4 E-G show unfolded microscopic octahedra, truncated tetrahedra, and crown microstructures (pretreated with O₃), respectively. Upon exposure to H₂, the top PtO_x layers of the hinges were actuated leading to the folded structures [scanning electron micrograph (SEM) images in Fig. 4 E-G and SI Appendix, Fig. S12]. Overall, these results demonstrate how SCAs can harness gaseous environments to actuate shape changes in complex 3D microstructures.

The use of chemical catalytic pathways opens up additional modalities for actuation. For example, SCAs can be driven by ultraviolet (UV) illumination using O_3 generated photochemically

from O_2 (26). To demonstrate this approach, we exposed the SCAs to UV light (185 nm wavelength and 3.5 mW/cm² intensity of UV radiation) in a stream of gas containing O_2 (Fig. 4 H and I and I and I appendix, Fig. S13). Fig. 4I shows that upon UV illumination, the curvatures of SCAs illuminated in either 20 v%, 50 v%, or 99.8 v% O_2 balanced with O_2 changed by O_2 This demonstrates that SCAs can be driven by fuels that are generated via photochemical processes from the ambient atmosphere, opening up approaches to photochemically driven micromachines (27, 28). For example, similar to a sunflower (29), the actuation of SCAs using photochemically generated O_3 could be used to create reconfigurable optical metamaterials that orient solar reflectors or panels toward light to maximize the collection of solar energy.

Discussion

800

700

Overall, the SCAs reported herein—the first micron-scale chemical actuators with submicrometer bending radii and subsecond cycle times—can be actuated in dry environments at room temperature without the need for wiring or electrical power, opening the door to fresh ideas for the actuation of microdevices that are fueled by targeted gases. In particular, our results show how the kinetics of surface-catalyzed reactions can be exploited to create responses that are orders

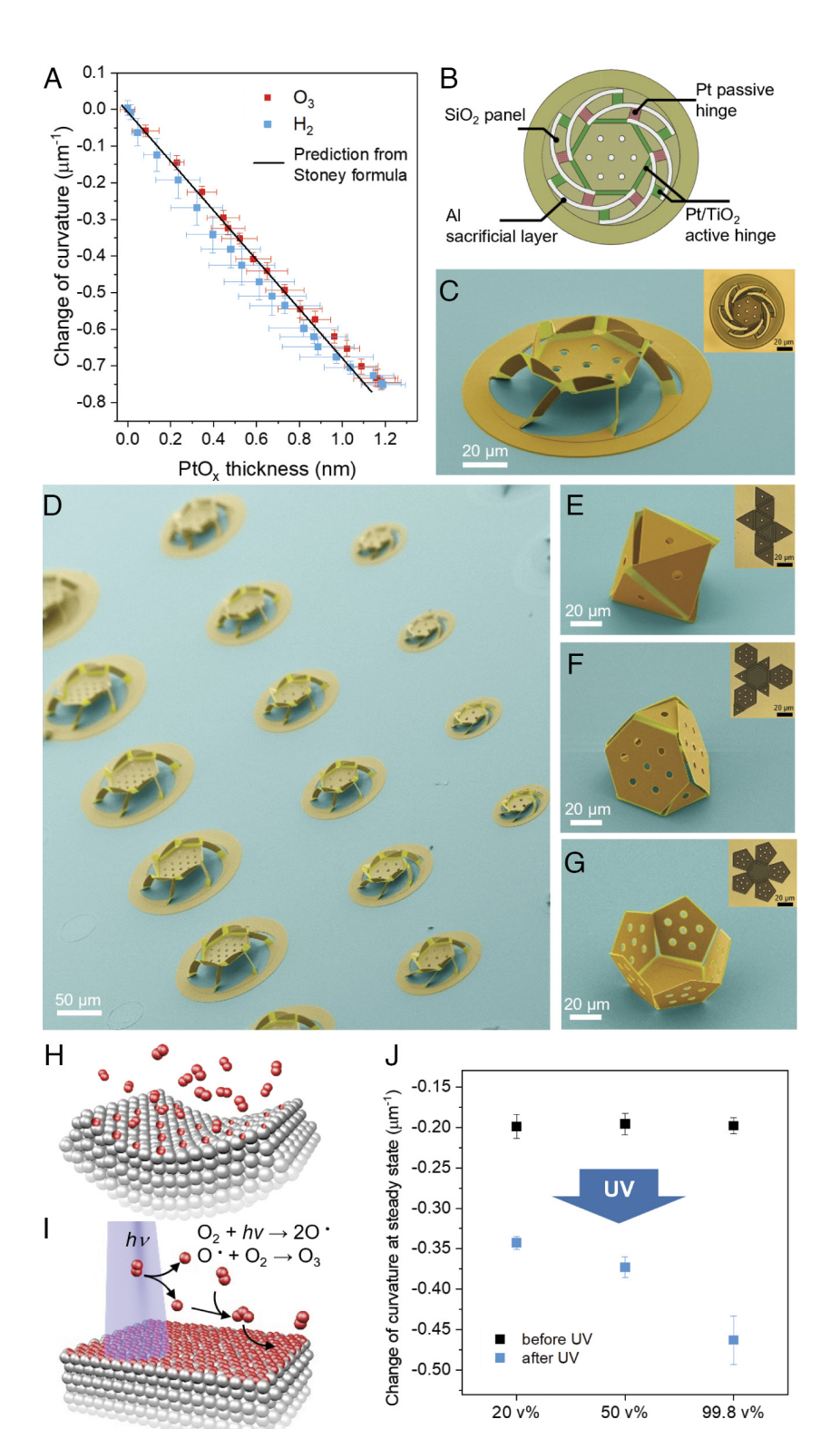


Fig. 4. Microdevices with complex structures driven by multiple SCAs. (A) Linear relationship between the curvature change of an SCA and thickness of the PtO_x layer on the Pt surface of the SCA during exposure to $1,290 \pm 40 \text{ ppm O}_3 \text{ (red) or } 2 \text{ v% H}_2 \text{ (blue)}$. The black line is a prediction from the Stoney formula (SI Appendix, Text). (B) Schematic illustration of a kirigami-based rotation microstage. (C and D) SEM images (false color) of kirigami-based rotation microstages. SEM images (false color) of origami-based (E) octahedra, (F) truncated tetrahedra, and (G) crown microstructures that were folded after 2 v% H_2 exposure. The *Insets* in (C and E-G) show optical images of unfolded microstructures (1,290 \pm 40 ppm O $_3$) prior to folding in H $_2$. Schematic illustration of the Pt surface exposed to O $_2$ without (H) and with (I) UV illumination. (J) Change of curvature (relative to 2 v% H₂) at steady state for SCAs in gaseous nitrogen streams containing either 20 v%, 50 v%, or 99.8 v% O₂ before (black) and after (blue) illumination with UV light for 10 min.

of magnitude faster and larger than prior demonstrations that have relied on equilibrated actuator surface states (6–11). We also demonstrate that long-lived oxide surface states can yield relatively stable structures. In the long term, we envisage designs of SCAs driven by changes in chemical environments generated during human respiration (30), plant photosynthesis, or atmospheric photochemical cycles associated with daily variation in the solar flux (27). Our results also suggest that it should be possible to design microactuators that exploit the coupling of reaction and diffusion to achieve self-regulated cycles from a steady flow of gaseous fuel (31–33). Lastly, because the SCAs

reported in our paper are fabricated in parallel with photolithographic processing, it is possible to integrate them into routine process flows that are used for fabrication of microsystems technologies such as microrobotics and medical microdevices.

Materials and Methods

O2 concentration

Fabrication of SCAs. We fabricated SCAs using a photolithographic approach (17). Briefly, the fabrication process involves patterning sacrificial layers, fabricating SiO_2 panels, patterning Pt/Ti bimorph hinges, releasing the panels

and hinges, and finally drying the resulting structures: i) To fabricate the sacrificial layers, we first evaporated 180 nm-thick Al and then grew 20 nm-thick Al₂O₃ using atomic layer deposition (ALD) at 110 °C on a borofloat glass. ii) To pattern the sacrificial layers, a positive photoresist (Microposit S1813 for ABM contact aligner) was spin-coated, and the pattern was defined photolithographically. iii) The sacrificial layers (Al and Al₂O₃) were then wet-etched in aluminum etchant type A, followed by stripping the photoresist. iv) To fabricate the device panel, a 500 nm-thick SiO₂ layer was deposited using plasma-enhanced chemical vapor deposition (PECVD, Oxford 100). v) A positive photoresist (Microposit S1813) was spin-coated and patterned. vi) The SiO₂ layer was etched by CHF₃/ O2 at 2,500 W using inductively coupled plasma etching (Oxford PlasmaLab 100), followed by stripping the photoresist. vii) Next, a 2 nm-thick layer of Ti was sputtered onto the substrate at 3 mTorr and 400 W. viii) We then grew a 7.5 nm-thick layer of Pt onto Ti using ALD. ix) A positive photoresist (Microposit S1813) was spin-coated, and the pattern was defined photolithographically. x) The Pt/Ti was then etched by an ion mill, followed by stripping the photoresist. xi) The devices were immersed in a basic developer AZ 726 MIF containing 2.38% tetramethylammonium hydroxide for several hours to etch the Al and Al₂O₃ sacrificial layers, thereby releasing the panel and the hinge from the substrate into the solution. xii) Before drying the devices, the samples were washed with deionized water and isopropanol sequentially. xiii) Finally, the samples were dried in a critical point drier (Leica CPD300). A schematic for the fabrication of a SCA is shown in SI Appendix, Fig. S1. The as-deposited Pt films possessed predominantly (111) crystallographic faces, as confirmed by X-ray diffraction (XRD) (SI Appendix, Fig. S2). The Ti was oxidized to TiO₂ upon exposure to ambient air (XPS in *SI Appendix*, Fig. S3). SCAs fabricated as described above possess a prestress between the Pt and TiO₂ (SI Appendix, Fig. S4), which leads to an initial curvature of the actuator (16, 17).

Electron Microscopy. High-resolution transmission electron microscopy (TEM) imaging. To image the cross-section of the SCA using TEM, a thin cross-sectional lamina was milled from the top of the sample using an ion beam (Helios G4 UX FIB, ThermoFisher Scientific). We then attached the sample to a copper TEM grid using a nanomanipulator. Lastly, the lamina was further thinned to electron transparency via a focused ion beam (FIB).

SEM imaging. The SCAs were sputtered with a thin layer of Au and imaged in the SEM (Zeiss Supra 55).

XRD. The crystallinity of Pt films was determined using XRD (Rigaku SmartLab X-ray diffractometer). The measurements were preformed using Cu-K α radiation with a wavelength of approximately 1.54 Å.

xps. Surfaces were analyzed using a Scienta Omicron ESCA-2SR with operating pressure ~1 × 10^{-9} Torr. Monochromatic Al K α x rays (1,486.6 eV) were used, and photoelectrons were collected from a 5 mm diameter analysis area. The photoelectrons were collected at a 0° emission angle with a source-to-analyzer angle of 54.7°. A pass energy of 200 eV was used for wide/survey scans, and 50 eV was used for high-resolution scans. All XPS results were analyzed by CasaXPS software.

Characterization of Actuation of SCA Devices by H_2 , O_3 , O_2 , or H_2/O_2 **Mixtures.** SCAs were exposed to a stream of nitrogen containing H_2 , O_2 , or H_2 / O₂ mixture, or air containing O₃ within a flow cell that was constructed to direct the gaseous flow across the SCAs while permitting observation using an optical microscope (Olympus CH40). The stream of gas containing H₂ was obtained from a certified cylinder containing 2 v% $\rm H_2$ in $\rm N_2$. The stream of gas containing O_2 was obtained from a certified cylinder containing 99.8 v% O_2 (~0.2 v% N_2). The O₃ stream was generated using an O₃ generator. For gas mixtures, H₂ and O2 gases with designed concentrations were mixed before being delivered to the flow cell. The gas fed to the flow cell was maintained at room temperature (20 °C). The flow rate of each gas stream was controlled using a rotameter (Aalborg Instruments and Control). The total flow rate was maintained at 500 mL min⁻¹ at atmospheric pressure. The videos of the actuation of SCAs were recorded using a Canon T6i camera.

Characterization of Actuation of SCAs Using O3 Generated Photochemically from O₂. SCAs and a UV light lamp (cold cathode) with 185 nm wavelength and 3.5 mW/cm² intensity of UV radiation (Join Optoelectronic Co.) were placed in a flow cell and then were exposed to 99.8 v%, 50 v%, or 20

 $v\% O_2$ balanced with N_2 (500 mL/min flow rate to maintain positive pressure in the exposure chamber).

Computational Methods. H_2 and O_2 reactions on Pt(111) were studied by means of periodic DFT calculations, employing the Perdew-Burke-Ernzerhof exchange-correlation functional (34) within the generalized gradient approach. The dispersion (van der Waals) term was approximated by the D3 correction as proposed by Grimme (35). All calculations were carried out using the Vienna ab initio simulation package (36), where the valence electron density is expanded by plane wave basis sets with an energy cutoff of 400 eV, while core electrons' contribution to the valence region is described by the projected augmented wave method (37). Pt(111) support slabs were modeled using 2×2 and 3×3 supercells for H₂ dissociation on 0.25 MLO*-covered Pt(111) and O₂ reactions on 1 ML H*-covered Pt(111), respectively. For H_2 dissociation, a 2 \times 2 supercell is large enough to ensure that there is no interaction between adsorbates in adjacent supercells. The numerical integrations were carried out in reciprocal space using Monkhorst-Pack (38) meshes with $7 \times 7 \times 1$ and $5 \times 5 \times 1$ k-points for the 2×2 and 3×3 supercells, respectively.

For all supercells used here, all slabs were four atomic layers thick, where the two topmost are allowed to relax, and the two bottommost are frozen in their bulk lattice positions. The minimum energy lattice parameter for bulk Pt was computed to be 3.97 Å, which compares well with the experimental value (3.92 Å) (39). The structural optimization was ensured by converging forces acting on the atoms to below 0.01 eV Å⁻¹. All calculations involving O₂ or derivative intermediates were performed spin-polarized. All converged structures were characterized by vibrational analysis through Hessian matrix diagonalization, where the matrix elements were obtained by finite differences of analytical gradients with displacements of 0.015 Å. The transition state (TS) structures were acquired using the climbing-image nudged-elastic-band method (40) employing seven intermediate images. The converged TS structures were further characterized by appropriate frequency analysis. Finally, all reported reaction energies were calculated considering H₂ and O₂ gas-phase species as reference and adding the zero-point energy contribution within the harmonic approximation.

The stability of configurations of H*-covered Pt(111) was investigated following an approach described in the literature (41-44). SI Appendix, Fig. S5 presents the temperature-pressure-dependent surface energies for surface H* coverages on Pt(111) not exceeding 1.25 ML. A surface coverage of 1.0 ML of H* is predicted under experimental conditions of 293 K and a H₂ partial pressure of 0.02 bar. Temperature and pressure dependencies on zero-point corrected H*-covered Pt(111) configuration energies were applied using tabulated experimental data (43).

Data, Materials, and Software Availability. All study data are included in the article and/or SI Appendix.

ACKNOWLEDGMENTS. This work was supported by the Cornell Center for Materials Research (DMR-1719875), the Army Research Office (ARO W911NF-18-1-0032), the NSF (EFMA-1935252) the Air Force Office of Scientific Research (MURI: FA9550-16-1-0031), and the Kavli Institute at Cornell for Nanoscale Science. The theoretical work was supported by Department of Energy-Basic Energy Sciences, Division of Chemical Sciences, grant DE-FG02-05ER15731. The computations were performed in part by using National Energy Research Scientific Computing Center (NERSC) resources, supported by the U.S. Department of Energy, Office of Science, under contract DE-AC02-05CH11231 (NERSC award BES-ERCAP0019973). Experimental work was performed in part at the Cornell NanoScale Facility, a National Nanotechnology Coordinated Infrastructure (NNCI) member supported by NSF Grant NNCI-2025233.

Author affiliations: "Smith School of Chemical and Biomolecular Engineering, Cornell University, Ithaca, NY 14853; "Laboratory of Atomic and Solid-State Physics, Cornell University, Ithaca, NY 14853; "Department of Chemical and Biological Engineering, University of Wisconsin-Madison, Madison, WI 53706; "Gibley School of Mechanical and Aerospace Engineering, Cornell University, Ithaca, NY 14853; "School of Applied and Engineering Physics, Cornell University, Ithaca, NY 14853; and Kavli Institute at Cornell for Nanoscale Science, Cornell University, Ithaca, NY 14853

Author contributions: N.B., Q.L., M.F.R., D.A.M., M.M., I.C., P.L.M., and N.L.A. designed research; N.B., Q.L., M.F., E.S., W.W., and M.C.C. performed research; N.B., Q.L., M.F.R., D.A.M., M.M., I.C., P.L.M., and N.L.A. analyzed data; and N.B., Q.L., I.C., P.L.M., and N.L.A. wrote the paper.

- B. C. H. Steele, A. Heinzel, Materials for fuel-cell technologies. Nature 414, 345-352 (2001).
- J. Heywood, Internal Combustion Engine Fundamentals (McGraw-Hill Education, 1988).
- X. He et al., Synthetic homeostatic materials with chemo-mechano-chemical self-regulation. Nature
- W. F. Paxton et al., Catalytic nanomotors: Autonomous movement of striped nanorods. J. Am. Chem. Soc. 126, 13424-13431 (2004).
- R. D. Vale, R. A. Milligan, The way things move: Looking under the hood of molecular motor proteins. Science **288**, 88-95 (2000).
- J. Biener et al., Surface-chemistry-driven actuation in nanoporous gold. Nat. Mater. 8, 47–51 (2009).
- H. P. Lang et al., A chemical sensor based on a micromechanical cantilever array for the identification of gases and vapors. Appl. Phys. A 66, S61–S64 (1998).
- D. R. Baselt et al., Design and performance of a microcantilever-based hydrogen sensor. Sensors Actuators B: Chem. 88, 120–131 (2003).
- S. J. McKeown, X. Wang, X. Yu, L. L. Goddard, Realization of palladium-based optomechanical cantilever hydrogen sensor. Microsyst. Nanoeng. 3, 16087 (2017).
- R. Berger et al., Surface stress in the self-assembly of alkanethiols on gold. Science 276, 2021–2024 (1997).
- J. S. Randhawa, M. D. Keung, P. Tyagi, D. H. Gracias, Reversible actuation of microstructures by surface-chemical modification of thin-film bilayers.pdf. Adv. Mater. 22, 407-410 (2010).
- K. Christmann, G. Ertl, T. Pignet, Adsorption of hydrogen on a Pt(111) surface. Surf. Sci. 54, 365-392
- C. Sachs, M. Hildebrand, S. Völkening, J. Wintterlin, G. Ertl, Spatiotemporal self-organization in a surface reaction: From the atomic to the mesoscopic scale. *Science* **293**, 1635–1638 (2001).
- J. L. Gland, B. A. Sexton, G. B. Fisher, Oxygen interactions with the Pt(111) surface. Surf. Sci. 95, 587-602 (1980).
- N. A. Saliba, Y. L. Tsai, C. Panja, B. E. Koel, Oxidation of Pt (111) by ozone (O₃) under UHV conditions. Surf. Sci. 419, 79-88 (1999).
- M. Z. Miskin et al., Electronically integrated, mass-manufactured, microscopic robots. Nature 584, 557-561 (2020).
- Q. Liu et al., Micrometer-sized electrically programmable shape-memory actuators for low-power microrobotics. Sci. Robot. 6, eabe6663 (2021).
- S. Alayoglu, A. U. Nilekar, M. Mavrikakis, B. Eichhorn, Ru-Pt core-shell nanoparticles for preferential oxidation of carbon monoxide in hydrogen. Nat. Mater. 7, 333-338 (2008).
- P. R. Norton, J. A. Davies, T. E. Jackman, Absolute coverages of CO and O on Pt(111); comparison of saturation CO coverages on Pt(100), (110) and (111) surfaces. Surf. Sci. Lett. 122, L593-L600 (1982).
- 20. N. M. Marković, T. J. Schmidt, V. Stamenković, P. N. Ross, Oxygen reduction reaction on Pt and Pt bimetallic surfaces: A selective review. Fuel Cells 1, 105-116 (2001).
- Y. Xu, A. V. Ruban, M. Mavrikakis, Adsorption and dissociation of O₂ on Pt-Co and Pt-Fe alloys. J. Am. Chem. Soc. 126, 4717-4725 (2004).
- 22. A. Michaelides, P. Hu, Catalytic water formation on platinum: A first-principles study. J. Am. Chem. Soc. 123, 4235-4242 (2001).

- 23. D. Fantauzzi et al., Growth of stable surface oxides on Pt(111) at near-ambient pressures. Angew Chemie Int. Ed. 56, 2594-2598 (2017).
- A. Bytnerowicz et al., Summer-time distribution of air pollutants in Sequoia National Park, California Environ. Pollut. 118, 187-203 (2002).
- Z. Wang, S. F. Kowal, N. Carslaw, T. F. Kahan, Photolysis-driven indoor air chemistry following cleaning of hospital wards. Indoor Air 30, 1241-1255 (2020).
- B. Eliasson, U. Kogelschatz, Ozone generation with narrow-band UV radiation. Ozone Sci. Eng. 13, 365-373 (1991).
- C. George, M. Ammann, B. D'Anna, D. J. Donaldson, S. A. Nizkorodov, Heterogeneous
- photochemistry in the atmosphere. Chem. Rev. 115, 4218-4258 (2015).
- J. Schneider et al., Understanding TiO₂ photocatalysis: Mechanisms and materials. Chem. Rev. 114, 9919-9986 (2014).
- H. S. Atamian et al., Circadian regulation of sunflower heliotropism, floral orientation, and pollinator visits. Science 353, 587-590 (2016).
- A. J. Berger, M. P. Hlastala, *Physiology of Respiration* (Oxford University Press, 2001).
- S. Amano, S. Borsley, D. A. Leigh, Z. Sun, Chemical engines: Driving systems away from equilibrium through catalyst reaction cycles. Nat. Nanotechnol. 16, 1057-1067 (2021).
- R. Imbihl, G. Ertl, Oscillatory kinetics in heterogeneous catalysis. Chem. Rev. 95, 697-733 (1995).
- S. Li et al., Self-regulated non-reciprocal motions in single-material microstructures. Nature 605,
- J. P. Perdew, K. Burke, M. Ernzerhof, Generalized gradient approximation made simple. Phys. Rev. Lett. 77, 3865-3868 (1996).
- S. Grimme, J. Antony, S. Ehrlich, H. Krieg, A consistent and accurate ab initio parametrization of density functional dispersion correction (DFT-D) for the 94 elements H-Pu. J. Chem. Phys. 132, 154104 (2010).
- G. Kresse, J. Furthmüller, Efficient iterative schemes for ab initio total-energy calculations using a plane-wave basis set. *Phys. Rev. B Condens. Matter Mater. Phys.* **54**, 11169-11186 (1996). P. E. Blöchl, Projector augmented-wave method. *Phys. Rev. B* **50**, 17953–17979 (1994).
- H. J. Monkhorst, J. D. Pack, Special points for Brillouin-zone integrations. Phys. Rev. B 13, 5188-5192 (1976).
- W. M. Haynes, CRC Handbook of Chemistry and Physics (CRC Press, 2015).
- G. Henkelman, B. P. Uberuaga, H. Jónsson, A climbing image nudged elastic band method for finding saddle points and minimum energy paths. J. Chem. Phys. 113, 9901-9904 (2000).
- M. V. Bollinger, K. W. Jacobsen, J. K. Nørskov, Atomic and electronic structure of MoS₂ nanoparticles. Phys. Rev. B 67, 085410 (2003).
- N. Moll, A. Kley, E. Pehlke, M. Scheffler, GaAs equilibrium crystal shape from first principles. Phys. Rev. B 54, 8844-8855 (1996).
- J. Greeley, M. Mavrikakis, A first-principles study of surface and subsurface H on and in Ni(111): Diffusional properties and coverage-dependent behavior. *Surf. Sci.* **540**, 215-229 (2003). M. Chase, *NIST-JANAF Thermochemical Tables* (American Institute of Physics, ed. 4, 1998).